Cognitive Neurodynamics (2022) 16:1221–1231
https://doi.org/10.1007/s11571-021-09764-0

RESEARCH ARTICLE

Electromagnetic induction effects on electrical activity within a memristive Wilson neuron model

Quan Xu[1] · Zhutao Ju[1] · Shoukui Ding[1] · Chengtao Feng[1] · Mo Chen[1] · Bocheng Bao[1]

Received: 15 April 2021 / Revised: 11 October 2021 / Accepted: 22 November 2021 / Published online: 20 January 2022

Abstract

Neurons can exhibit abundant electrical activities due to physical effects of various electrophysiology environments. The electromagnetic induction flows can be triggered by changes in neuron membrane potential, which can be equivalent to a memristor applying on membrane potential. To imitate the electromagnetic induction effects, we propose a three-variable memristor-based Wilson neuron model. Using several kinetic analysis methods, the memristor parameter- and initial condition-related electrical activities are explored intensively. It is revealed that the memristive Wilson neuron model can display rich electrical activities, including the asymmetric coexisting electrical activities and antimonotonicity phenomenon. Finally, using off-the-shelf discrete components, an analog circuit on a hardware level is implemented to verify the numerically simulated coexisting electrical activities. Studying these rich electrical activities in neurons can build the groundwork to widen the neuron-based engineering applications.

Keywords Coexisting electrical activities · Antimonotonicity · Memristive electromagnetic induction · Analog circuit implementation · Wilson neuron model

Introduction

In perspective, the ions transmission plays an important role of information coding and dealing in biological neuron. Thus, many mathematical neuron models have been built by mainly considering the interaction between ion channel currents and membrane potential (Hodgkin and Huxley 1952; Morris and Lecar 1981; Chay 1985; Wilson 1999; Bao et al. 2020a; Xu et al. 2020). Under these considerations, the physical effect of different electrophysiology environments should be taken into account during the modeling of neuronal activities (Wang et al. 2017; Ye et al. 2018; Xu et al. 2019; Yang et al. 2020). Especially, the electrical field and its induced current can result by the change of membrane potential during the exchange of intracellular ions and extracellular ions (Lv et al. 2016). Therefore, the effect of electromagnetic induction caused by inner electrical field fluctuation should be considered in exploring the neuronal activities. That is to say, the electromagnetic induction participates and affects the electrical activity in a neuron. Ma et al. comes up with the idea that the magnetic flux can be employed to describe the electromagnetic induction in the neuron (Ma and Tang 2017) according to the Maxwell's electromagnetic induction theorem (Carpenter 1999). The flux-controlled memristor is one category of memristor and its memductance is really dependent on its crossing flux (Chua 2015; Xu et al. 2016). The state equation of the flux-controlled memristor can be restricted by its magnetic flux variation rate and applying voltage. This is very similar to the interaction between the electromagnetic induction and membrane potential of the biological neuron. Thus, the flux-controlled memristor can be reasonably employed to unify the physical effect of electromagnetic physiology in the media of neuron (Wu et al. 2016; Parastesh et al. 2018). Up to now, following the pioneer achievements (Lv et al. 2016; Wu et al. 2016), some fascinating neuron models with the consideration of memristive electromagnetic induction have been raised (Ge et al. 2018; Rostami and Jafari 2018; Bao et al. 2018b; Jin et al. 2019; Kafraj et al. 2020; An and Qiao 2021).

✉ Bocheng Bao
mervinbao@126.com

[1] School of Microelectronics and Control Engineering, Changzhou University, Changzhou 213164, People's Republic of China

By introducing the flux-controlled memristor into Hodgkin-Huxley neuron model to emulate the electromagnetic induction flow, dynamical responses with different modes and stochastic resonance were observed (Wang et al. 2017). And then, the electromagnetic induction effects on the regulation of sleep wake cycle were further studied in a simple wake-sleep neural network coupled by glutamate synapse. It was found that the average firing frequency can be modified by the intensity of electromagnetic induction (Jin et al. 2019). Besides, the memristive electromagnetic induction was considered in Hindmarsh-Rose neuron model. These modes of electrical activities can be softly altered with respect to the induced current that depends on the variation of magnetic flow (Lv et al. 2016; Mondal et al. 2019). With comprehensive consideration of the electromagnetic induction and radiation, high and low frequency stimulus, and Gaussian white noise, mode transition of electrical activities and thought-provoking phenomena were explored by bifurcation analysis (Ge et al. 2018). Furthermore, employing a discontinuous flux-controlled memristor as electromagnetic induction, a modified Hindmarsh-Rose neuron model was derived, within which chaotic and hyperchaotic dynamical behaviors were explored (Parastesh et al. 2018). After that, to mimic the threshold effect of electromagnetic induction, a threshold flux-controlled memristor-based Hindmarsh-Rose neuron model was presented, from which the coexisting hidden bursting patterns were revealed (Bao et al. 2020b). Besides, the electrical mode transition in hybrid Hindmarsh-Rose and Wilson neuron models with the consideration of electromagnetic induction was investigated (Liu et al. 2019). In addition, the coexisting firing patterns and initial-dependent bifurcation routes were disclosed in two adjacent Hindmarsh-Rose neurons coupled by memristive electromagnetic induction, within which the electromagnetic induction was caused by the membrane potential difference between two neurons (Bao et al. 2018b). Beyond these explorations, there still exist some unsolved and valuable works in this pregnant issue.

Summarily, most of these explorations are numerically executed on conductance-independent neuron models, which are described by simple mathematical model to express some specific behaviors without the consideration of neuron physiological structures (FitzHugh 1961; Hindmarsh and Rose 1982). But the conductance-dependent neuron models are more precisely able to imitate the neuronal activities with electrophysiological characteristics of the neuron membrane potential and ion currents (Hodgkin and Huxley 1952). Following this work, Wilson built a more realistic four-variable neuron model in which its ion conductances have quadratic polynomial forms to restrict the dynamics to cubic nonlinearities (Wilson 1999). Firing patterns and their forming mechanisms in the four-variable Wilson neuron model were further revealed in depth (Qi et al. 2013). Thereafter, a three-variable Wilson neuron model was projected by taking no account of the calcium ion current (Zhao et al. 2013; Liu et al. 2019). Furthermore, without regarding the calcium ion current and calcium ion mediated potassium ion hyperpolarizing current, a two-variable Wilson neuron model was employed to investigate the white-noise induced susceptibility (Steyn-Ross et al. 2006) and then to explore the spatial coarse-graining of spiking dynamics using a spatial blocking technique (Steyn-Ross and Steyn-Ross 2016).

In this paper, we consider a conductance-dependent three-variable Wilson neuron model with the memristive electromagnetic induction described by a flux-controlled memristor with the memductance of absolute function. The adopted memductance function is different from the previously employed quadratic function [i.e. $W(\varphi) = \alpha + \beta\varphi^2$ (Wang et al. 2017)] and hyperbolic tangent function [i.e. $W(\varphi) = \tanh\varphi$ (Bao et al. 2020b)]. Abundant electrical activities, coexisting electrical behaviors, and antimonotonicity phenomenon are numerically disclosed by dynamics exploration. The two-variable Wilson neuron model can be digitally realized on FPGA platform by approximately implementing the nonlinearity with a piecewise linear function (Imani et al. 2019; Nouri et al. 2019). Beyond the digital realization, the analog circuit implementation for neuron model is more suitable for the integrated circuit design of neuron network (Pinto et al. 2000) and can effectively promote some diverse neuron-based engineering applications (Jiang et al. 2018). What's more, the analog circuit implementation can involve the physical effects of parasitic parameters and display physical rather than numerical firing activities. Thus, the neuron model should first be implemented in a physical hardware platform. To this end, an electronic neuron for the proposed memristive Wilson neuron model is implemented by analog circuit and hardware measurements are executed to verify the numerically revealed electrical activities.

The remainder of this paper is organized as follows. A memristive Wilson neuron model is obtained by considering the electromagnetic induction, and then the memristor parameter- and initial condition-related dynamical behaviors are revealed by numerical simulations. Furthermore, the analog circuit-based hardware implementation and experimental measurements are executed. Finally, the conclusion is drawn.

Memristive Wilson neuron model

The two-variable Wilson neuron model was firstly simplified from the Hodgkin-Huxley model (Wilson 1999), which is mathematically described as

$$C_{\mathrm{m}}\frac{\mathrm{d}v}{\mathrm{d}\tau} = -m_{\infty}(v)(v - E_{\mathrm{Na}}) - g_{\mathrm{K}}r(v - E_{\mathrm{K}}) + I, \tag{1a}$$

$$\frac{\mathrm{d}r}{\mathrm{d}\tau} = \frac{1}{\tau_r}(-r + r_{\infty}(v)), \tag{1b}$$

where v denotes the membrane potential and r determines the recovery variable. I is an externally applied steady current. $m_{\infty}(v)$ denotes the Na^{+} ion activation function and $r_{\infty}(v)$ represents the equation state of recovery variable. The forms for $m_{\infty}(v)$ and $r_{\infty}(v)$ are expressed as

$$\begin{aligned} m_{\infty}(v) &= 17.8 + 47.6v + 33.8v^2, \\ r_{\infty}(v) &= 1.24 + 3.7v + 3.2v^2. \end{aligned} \tag{2}$$

The flux-controlled memristors with the memductances of quadratic function (Liu et al. 2019) and tangent function (Bao et al. 2020b) have been used to describe the electromagnetic induction flows. These memristors used are all with smooth nonlinear memductance functions. To perform the non-smooth impacts in the electromagnetic environment, a flux-controlled memristor with absolute function memductance $W(\varphi) = a - b|\varphi|$ is employed to imitate the electromagnetic induction effect on the membrane potential. Then, a memristive Wilson neuron model is constructed by replacing the externally applied steady current with the current generated by the memristor. The memristive Wilson neuron model is mathematically obtained by

$$C_{\mathrm{m}}\frac{\mathrm{d}v}{\mathrm{d}\tau} = -m_{\infty}(v)(v - E_{\mathrm{Na}}) - g_{\mathrm{K}}r(v - E_{\mathrm{K}}) + k(a - b|\varphi|)v, \tag{3a}$$

$$\tau_r\frac{\mathrm{d}r}{\mathrm{d}\tau} = -r + r_{\infty}(v), \tag{3b}$$

$$\tau_{\varphi}\frac{\mathrm{d}\varphi}{\mathrm{d}\tau} = k_1 v - \varphi, \tag{3c}$$

within which φ is the flux variable of the memristor and k is the electromagnetic induction coupling strength. The electromagnetic induction current $I_{M} = kW(\varphi)v = k(a - b|\varphi|)v$ is regulated by the variation of magnetic flux. The proposed neuron model (3) is a purely mathematical description and its dimensionless model parameters are properly selected as listed in Table 1. Note that the membrane potential v has been scaled to units of mV/100 to restrict the constants in Eq. (2) within a reasonable range (Wilson 1999; Liu et al. 2019). For the sake of simplicity, dimensionless parameters are used in the following numerical simulations.

Parameter- and initial condition-related electrical activity

When the coupling strength k is selected as the adjustable parameter, the bifurcation plots for initial conditions $[v(0), r(0), \varphi(0)] = (0, 1, 0)$ and $(0, -1, 0)$ are illustrated. MATLAB ODE45 algorithm with fixed time-step 0.01 and time-interval [0.99, 1] is utilized to plot bifurcation diagrams and Wolf's Jacobi method (Wolf et al. 1985) with time-step 1 and time-end 20 is utilized to calculate the finite-time Lyapunov exponents.

To disclose the electrical activities in model (3), one-dimensional (1D) bifurcation diagrams and finite-time Lypunov exponents are plotted in Fig. 1a, b, respectively. In Fig. 1a, the trajectories colored in red and deep green are triggered by the initial conditions $[v(0), r(0), \varphi(0)] = (0, -1, 0)$ and $(0, 1, 0)$, respectively. The top figure of Fig. 1a shows the bifurcation diagram in the region of $k = [5, 10]$ and the bottom figure gives a partial enlargement diagram covering the range of $k = [9, 10]$. The top and bottom figures in Fig. 1b give the finite-time Lyapunov exponents for the two sets of initial conditions, respectively.

In Fig. 1a, the bifurcation diagrams show that the neuron model (3) can generate abundant mode transition and asymmetric coexistence of electrical activities as electromagnetic induction coupling strength k is varied. By these numerical simulations, it is found that the asymmetric coexisting electrical activities are only triggered by large values of coupling strength k, i.e. $k \geq 9.056$. These electrical activities are further confirmed by the finite-time Lyapunov exponents depicted in Fig. 1b. Specially, the region marked by I in Fig. 1b corresponds to the asymmetric coexisting behaviors (Bao et al. 2018a) for the two sets of initial conditions. It is also revealed that periodic and chaotic electrical activities occur with the variation of the coupling strength k. To confirm these electrical activities, four discrete values of k are selected to numerically plot their phase portraits and sequences as shown in Fig. 2. These are periodic electrical activity for $k = 6$, chaotic electrical activity for $k = 8.5$, coexisting periodic and chaotic electrical activities for $k = 9.1$, and coexisting periodic electrical activities for $k = 9.8$, respectively.

To further disclose the electrical activities, two-dimensional (2D) bifurcation diagrams depicted by checking the periodicities of the membrane potential v under the two sets of initial conditions $[v(0), r(0), \varphi(0)] = (0, -1, 0)$ and $(0, 1, 0)$ are drawn in the $k - \tau_{\varphi}$ parameter plane, as shown in Fig. 3a, b, respectively.

In Fig. 3, the marks with different colors on the colorbar located at the right-hand side are utilized to identify the different electrical activities, among which the color labeled by CH denotes chaotic electrical activity and the other colors labeled by P01–P08 represent the periodic electrical activities with different periodicities of period-1 to period-8 respectively. It is revealed that the memristive Wilson neuron model can generate periodic electrical activities with different periodicities and chaotic electrical activities. At first glance, the electrical activities revealed

Table 1 Dimensionless parameter values and significations of the memristive Wilson neuron model (Color table online)

Parameters	Significations	Values
C_m	membrane capacitor	1
E_{Na}	reversal potential of Na^+ ion channel	0.5
E_K	reversal potential of K^+ ion channel	–0.95
g_K	the maximal conductance of K^+ ion channel	26
τ_r	channel activation time constant of the K^+ ion	5
τ_φ	time scale of the flux variation	0.5
a	memristor inner constant parameter	1
b	flux-related memductance changing rate	3
k	electromagnetic induction coupling strength	6
k_1	time scale coefficient	1

by 2D bifurcation diagrams for the two sets of initial conditions are very similar. But there exist some differences by carefully checking the electrical activities in the k – τ_φ parameters plane, as shown in Fig. 4.

In Fig. 4, the marks with different colors on the colorbar are utilized to identify the differences of coexisting behaviors, among which the grey color labeled by 00 denotes the unanimous coexisting behaviors and the other colors labeled by 01–08 represent the occurrence of different asymmetric coexisting behaviors for the same parameters. i.e. 07 represents the asymmetric coexistence of period-2 and chaos or asymmetric coexistence of period-1 and period-8. Figure 4 is numerically obtained by checking the electrical activities with respect to k and τ_φ for the two sets of initial conditions. Besides, the differences of the coexisting behaviors become more pronounced as the labeled number increased, which imply that there exist abundant asymmetric coexisting electrical activities in the proposed memristive Wilson neuron model.

It is revealed that the neuron model (3) can generate rich asymmetric coexisting behaviors under the two sets of initial conditions. Herein, to further reveal the initial conditions-related asymmetric coexisting electrical activities, four sets of model parameters belonging to four different regions of Fig. 4 are selected as examples to demonstrate the asymmetric coexisting behaviors by local attraction basins (Gu et al. 2015), as shown in Fig. 5. The local attraction basins are plotted with the initial conditions φ_0 and r_0 varying in the range of $[-2, 2]$, respectively. The neuron model (3) supports rich asymmetric coexisting behaviors as illustrated in Fig. 5. It can generate the coexisting limit cycle with period-3 and chaotic electrical activities for $k = 8.5$ and $\tau_\varphi = 0.7$ and coexisting limit cycle with period-4 and chaotic electrical activities for $k = 8.8$ and $\tau_\varphi = 0.48$ as shown in Fig. 5a, b, respectively. Figure 5c, d illustrate the coexistence of limit cycles with period-1 and period-5 electrical activities for $k = 9.5$ and $\tau_\varphi = 0.36$, as well as the coexistence of limit cycles with period-2 and period-3 electrical activities for $k = 9.8$ and $\tau_\varphi = 0.56$, respectively. To present the asymmetric coexisting electrical activities more explicitly, phase portraits and sequences for the four sets of model parameters are plotted in Fig. 6. The initial conditions for the red and dark green traces are the same as those utilized in Fig. 2.

Antimonotonicity phenomenon

The antimonotonicity phenomenon of generating and annihilating periodic orbits (Dawson et al. 1992) is also observed with the variation of coupling strength k. The antimonotonicity phenomenon has been revealed in memristive Twin-T oscillator (Zhou et al. 2018), Jerk circuit (Kengne et al. 2017), and non-autonomous series–parallel inductor-capacitor circuit (Manimehan and Philominathan 2012), just to refer a few. The existence of periodic islands in the parameter space is the essential condition to develop period-doubling and reverse period-doubling bifurcations (Xu et al. 2016).

According to numerous numerical simulations, the antimonotonicity phenomenon is found under another set of model parameters. To demonstrate the evolution of the antimonotonicity phenomenon in the neuron model (3), a set of bifurcation diagrams is drawn in Fig. 7 by adjusting k for three discrete values τ_φ. Other model parameters are specially fixed as $C_m = 1$, $E_{Na} = 0.5$, $E_K = -0.95$, $g_K = 26$, $\tau_r = 5$, $a = 0.5$, $b = 2$, and $k_1 = 1$. For $\tau_\varphi = 0.125$, two branches of chaotic bubbles are observed and the two branches individually develop themselves. As τ_φ decreasing, the chaotic bubbles evolve to period-4 bubble (i.e. $\tau_\varphi = 0.120$) and then to period-2 bubble (i.e. $\tau_\varphi = 0.118$). In a word, the chaotic bubbles gradually evolve to period-2 bubbles when decreasing τ_φ.

Hardware circuit implementation and experimental measurement

Electronic neurons in a hardware form are significant to develop applications in artificial neural networks (Bao et al. 2021). Thus, the proposed three-variable memristive Wilson neuron model (3) is synthesized by the off-the-shelf discrete components on an analog circuit level. Thereafter, the hardware circuit can be manually welded and experimental measurements can be thereby performed to confirm the numerically simulated electrical activities.

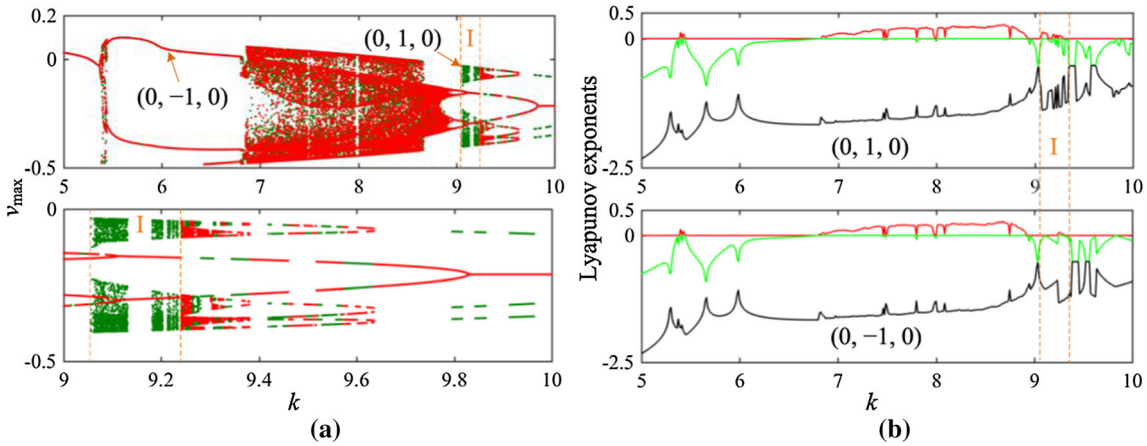

Fig. 1 Numerically simulated bifurcation diagrams of the maxima membrane potential v_{max} and the finite-time Lyapunov exponents with respect to k. **a** Bifurcation diagrams, **b** finite-time Lyapunov exponents (Color figure online)

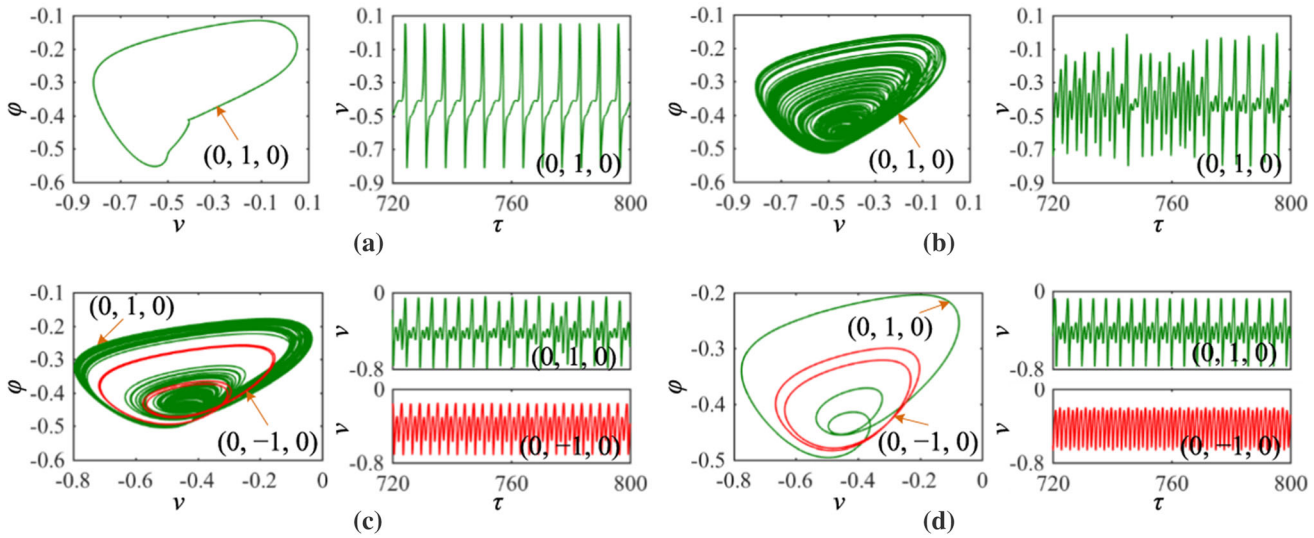

Fig. 2 Phase portraits in $v - \varphi$ plane and sequences for the membrane potential v with respect to some discrete value of k. **a** $k = 6$, **b** $k = 8.5$, **c** $k = 9.1$, **d** $k = 9.8$ (Color figure online)

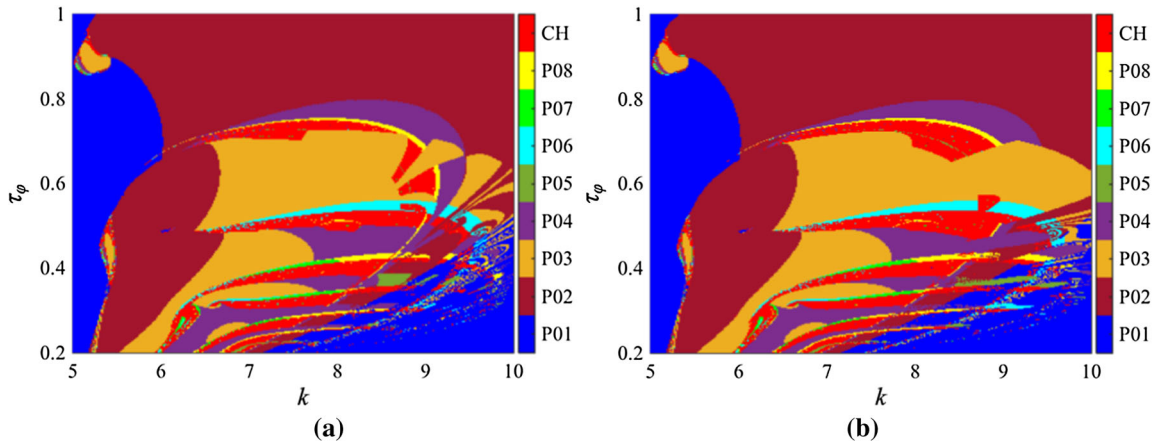

Fig. 3 Electrical activities revealed by 2D bifurcation diagrams in $k - \tau_\varphi$ parameter plane. **a** Initial conditions of $[v(0), r(0), \varphi(0)] = (0, 1, 0)$, **b** initial conditions of $[v(0), r(0), \varphi(0)] = (0, -1, 0)$ (Color figure online)

To reduce the number of discrete components in analog circuit implementation, we simplify the neuron model (3) with the typical model parameters as

$$\frac{dv}{d\tau} = 8.9 - 24.7r - 26vr + 6v - 30.7v^2 - 33.8v^3 + k(1-3|\varphi|)v, \tag{4a}$$

$$\frac{dr}{d\tau} = -0.2r + 0.74v + 0.64v^2 + 0.248, \tag{4b}$$

$$\frac{d\varphi}{d\tau} = \frac{1}{\tau_\varphi}(v-\varphi), \tag{4c}$$

where k and τ_φ are two adjustable parameters.

The analog circuit can be physically implemented according to the mathematical model given in (4). The memristor with absolute function memductance is implemented by employing the saturation characteristic of the operational amplifier U_b whose saturation voltage is E_{sat}. The memristor is realized as shown in the upper panel of Fig. 8. The describing equation of the flux-controlled memristor can be obtained as

$$RC\frac{dV_\varphi}{dt} = \frac{R}{R_1}V_v - \frac{R}{R_2}V_\varphi, \tag{5a}$$

$$i = -\left(\frac{1}{R_3} - \frac{g_a g_b E_{sat}}{R_4}|V_\varphi|\right)V_v, \tag{5b}$$

where $t = RC\tau$ is the physical time and RC is the integral time constant. g_a and g_b are the gains of analog multipliers M_a and M_b respectively.

The main circuit consists of two channels to integrate the two ordinary differential equations of (4a) and (4b) (Bao et al. 2017; Li et al. 2017], as drawn at the bottom of Fig. 8. The main circuit in Fig. 8 has two dynamic elements, corresponding to two state variables of V_v, and V_r.

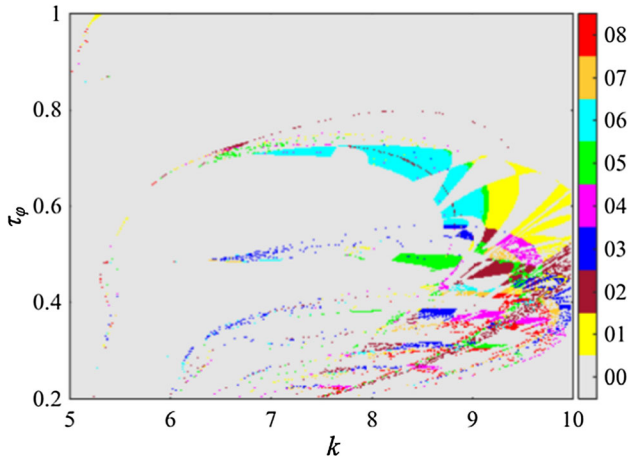

Fig. 4 The different coexisting behaviors in $k - \tau_\varphi$ parameter plane for the two sets of initial conditions $[v(0), r(0), \varphi(0)] = (0, -1, 0)$ and $(0, 1, 0)$. (Color figure online)

Therefore, the circuit state equations having the same integral time constant in (5) can be established as

$$RC\frac{dV_v}{dt} = -\frac{R}{R_5}V_1 - \frac{R}{R_6}V_r - \frac{g_3R}{R_7}V_vV_r + \frac{R}{R_8}V_v - \frac{g_2R}{R_9}V_v^2 - \frac{g_1g_2R}{R_{10}}V_v^3 + \left(\frac{R}{R_3} - \frac{g_ag_bE_{sat}R}{R_4}|V_\varphi|\right)V_v, \tag{6a}$$

$$RC\frac{dV_r}{dt} = -\frac{R}{R_{15}}V_r + \frac{R}{R_{17}}V_v + \frac{g_2R}{R_{16}}V_v^2 - \frac{R}{R_{18}}V_2, \tag{6b}$$

$$RC\frac{dV_\varphi}{dt} = \frac{R}{R_1}V_v - \frac{R}{R_2}V_\varphi, \tag{6c}$$

where g_1, g_2, and g_3, are the gains of analog multipliers M_1, M_2, and M_3, respectively, and V_1 and V_2 are two DC voltages.

Comparing (4) and (6), we can obtain

$$R_1 = \tau_\varphi R, R_2 = \tau_\varphi R, R_3 = \frac{R}{k}, R_4 = \frac{g_ag_bE_{sat}}{3k}R,$$
$$R_5 = -\frac{V_1}{8.9}R, R_6 = \frac{R}{24.7}, R_7 = \frac{g_3R}{26}, R_8 = \frac{R}{6}, R_9 = \frac{g_2R}{30.7},$$
$$R_{10} = \frac{g_1g_2}{33.8}R, R_{15} = \frac{R}{0.2}, R_{16} = \frac{g_2R}{0.64}, R_{17} = \frac{R}{0.74}, R_{18} = -\frac{V_2}{0.248}R. \tag{7}$$

Set the integral time constant as $RC = 0.1$ ms, i.e. $R = 10$ kΩ and $C = 10$ nF. The experimental measured saturation voltages of AD711JN are $E_{sat} = \pm 13.5$ V. The gains of analog multipliers are $g_a = 0.1$ V^{-1} and $g_b = g_1 = g_2 = g_3 = 1$ V^{-1}. The two DC voltages are selected as $V_1 = -8.9$ V and $V_2 = -0.248$ V. Thus, the resistances $R_5 \sim R_{18}$ are calculated as $R_5 = R_{11} = R_{12} = R_{13} = R_{14} = R_{18} = 10$ kΩ, $R_6 = 0.405$ kΩ, $R_7 = 0.385$ kΩ, $R_8 = 1.667$ kΩ, $R_9 = 0.326$ kΩ, $R_{10} = 0.296$ kΩ, $R_{15} = 50$ kΩ, $R_{16} = 15.625$ kΩ, and $R_{17} = 13.513$ kΩ. The resistances $R_1 \sim R_4$ are adjusted to meet the selected parameters k and τ_φ in the numerical simulations for observing the coexisting electrical activities.

With the circuit schematic in Fig. 8, an analog circuit is practically set up by commercially available off-the-shelf discrete components on a breadboard. The monolithic capacitors and precise potentiometers, as well as the operational amplifiers AD711JN and multipliers AD633JN with ± 15 V voltage supplies are employed. The experimental results are captured by a Tektronix four-channel digital oscilloscope. It is emphasized that the desired different initial capacitor voltages are difficult to accurately assign in the hardware circuit, which are randomly sensed through repeatedly turning on the hardware circuit power supplies (Xu et al. 2016; Bao et al. 2017). Luckily, the regions of attraction for the asymmetric coexisting electrical activities in local attraction basins are basically linked up into a big single stretch, which give us the

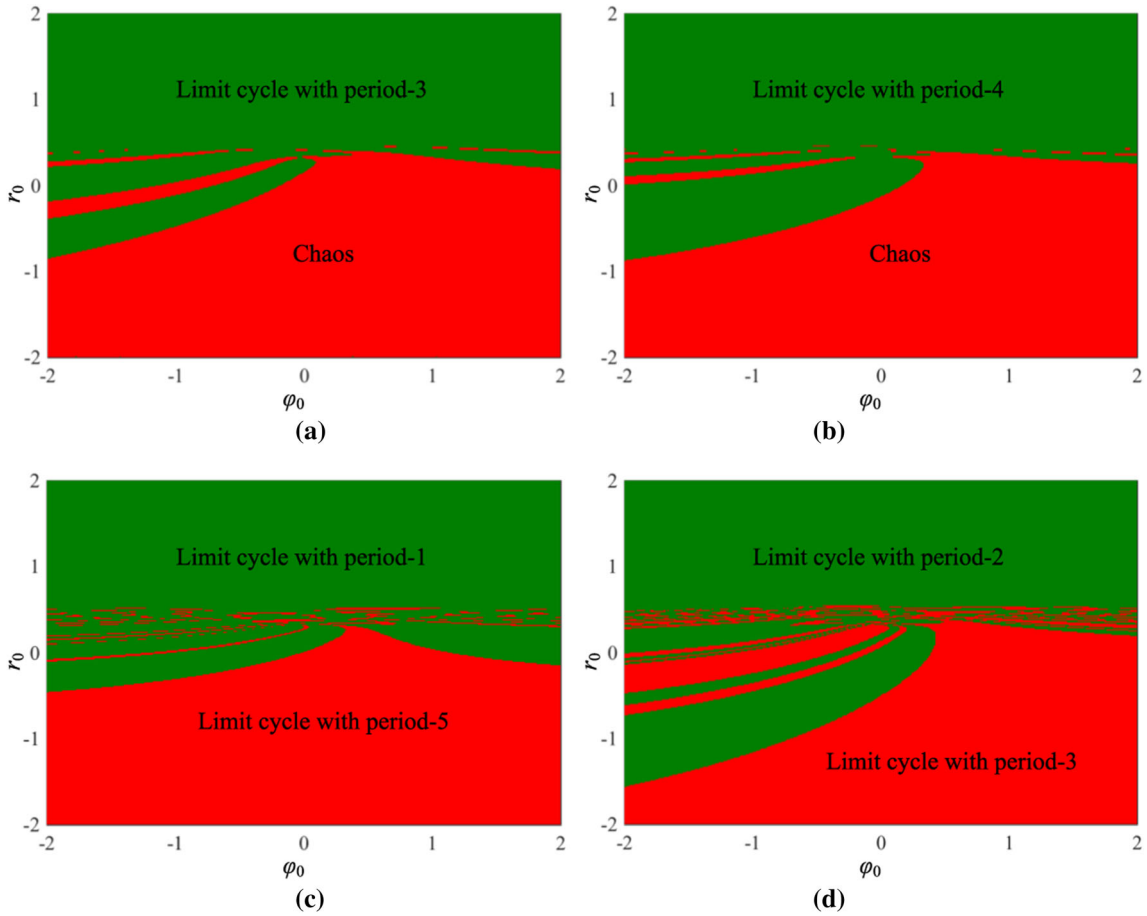

Fig. 5 Local attraction basins in the $\varphi_0 - r_0$ initial condition plane for different parameters. **a** $k = 8.5$ and $\tau_\varphi = 0.7$, **b** $k = 8.8$ and $\tau_\varphi = 0.48$, **c** $k = 9.5$ and $\tau_\varphi = 0.36$, **d** $k = 9.8$ and $\tau_\varphi = 0.56$ (Color figure online)

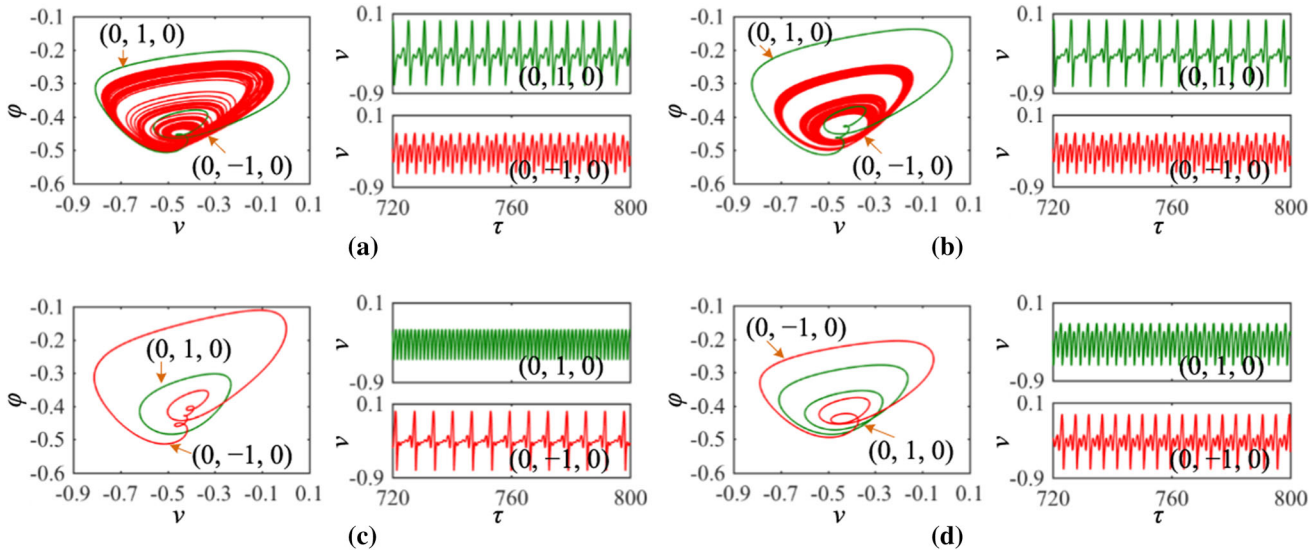

Fig. 6 Phase portraits in $v - \varphi$ plane and sequences for the membrane potential v with respect to the four sets values of k and τ_φ. **a** $k = 8.5$ and $\tau_\varphi = 0.7$, **b** $k = 8.8$ and $\tau_\varphi = 0.48$, **c** $k = 9.5$ and $\tau_\varphi = 0.36$, **d** $k = 9.8$ and $\tau_\varphi = 0.56$ (Color figure online)

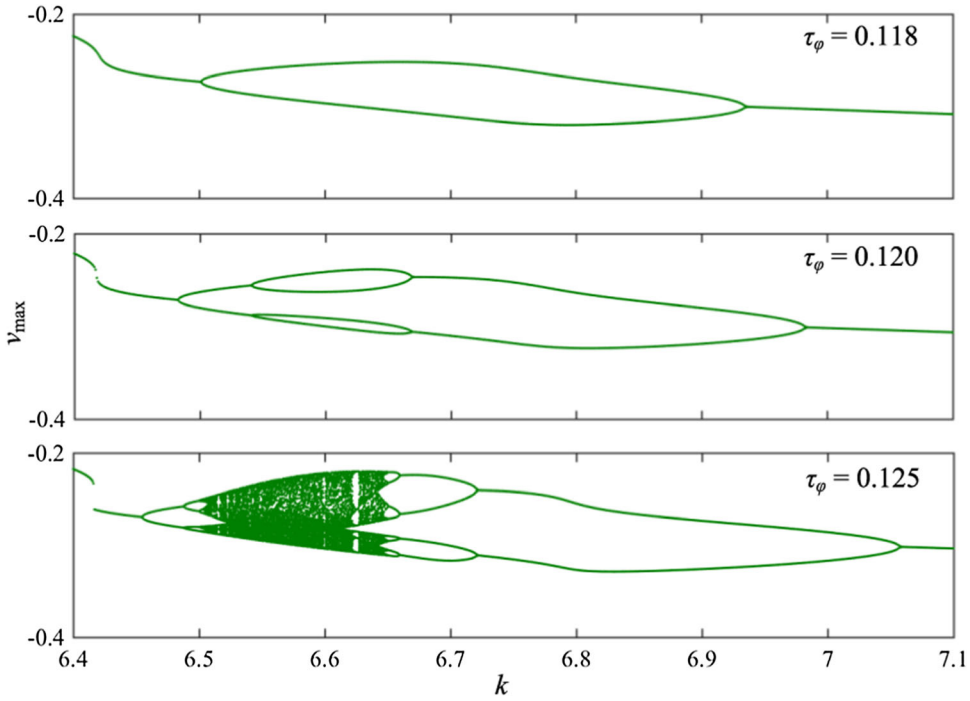

Fig. 7 Bifurcation diagrams of the maxima of the membrane potential v with respect to k for three discrete values of the time constant τ_φ. (Color figure online)

opportunity to easily sense the initial conditions belonging to these regions of local attraction basins.

To confirm the asymmetric coexisting electrical activities in hardware experiment, the theoretical values of resistors $R_1 \sim R_4$ are calculated to meet the selected four sets parameters k and τ_φ by Eq. (7). In the hardware experiments, only the four resistances $R_1 \sim R_4$ in the analog circuit can be tuned. Corresponding to the theoretical values (abbreviated as Theo. value) of the four resistances, the experimental values (abbreviated as Exp. value) of the four resistances are measured by Precision LCR Meter, as listed in Table 2. As can be seen, the theoretical and experimental resistances have some slight deviations. These slight deviations are caused by the model idealizations, parasitic parameters, measurement errors, and so on. The experimental values in hardware measurements can contribute to the adjustment of the electronic neuron in exploring its engineering applications. Corresponding to the phase trajectories and time-domain waveforms in Fig. 6, the asymmetric coexisting behaviors of limit cycle with period-3 and chaotic electrical activities, limit cycle with period-4 and chaotic electrical activities, limit cycles with period-1 and period-5 electrical activities, as well as limit cycles with period-2 and period-3 electrical activities are captured, as illustrated in Fig. 9a–d, respectively.

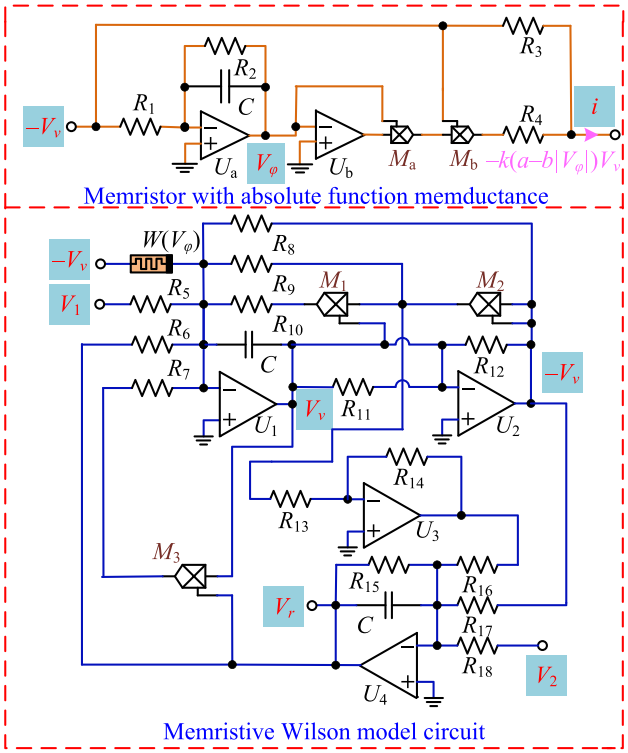

Fig. 8 Analog circuit schematic for implementing the memristive Wilson neuron model. (Color figure online)

Table 2 Theoretical values and experimental values of the four adjustable potentiometers (Color table online)

k	τ_φ	R_1/kΩ		R_2/kΩ		R_3/kΩ		R_4/kΩ	
		Theo. value	Exp. value	Theo. value	Exp. value	Theo. value	Exp. value	Theo. value	Exp. value
8.5	0.7	7	7.072	7	7.091	1.176	1.182	0.529	0.521
8.8	0.48	4.8	4.822	4.8	4.563	1.136	1.280	0.511	0.516
9.5	0.36	3.6	3.612	3.6	3.515	1.053	1.056	0.474	0.453
9.8	0.56	5.6	5.683	5.6	5.832	1.02	0.946	0.459	0.449

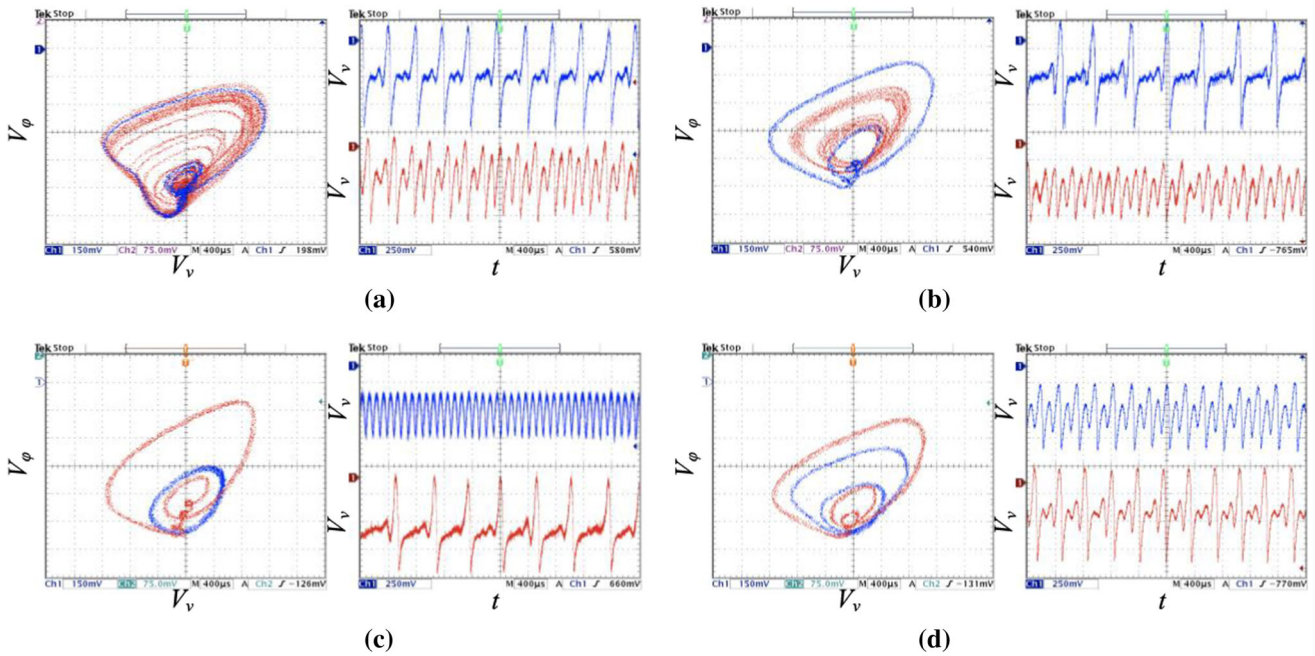

Fig. 9 The experimentally captured trajectories in $V_v - V_\varphi$ plane and time-domain waveforms for the four-representative coexisting electric activities. **a** $R_1 = 7.072$ kΩ, $R_2 = 7.091$ kΩ, $R_3 = 1.182$ kΩ, and $R_4 = 0.521$ kΩ, **b** $R_1 = 4.822$ kΩ, $R_2 = 4.563$ kΩ, $R_3 = 1.280$ kΩ, and $R_4 = 0.516$ kΩ, **c** $R_1 = 3.612$ kΩ, $R_2 = 3.515$ kΩ, $R_3 = 1.056$ kΩ, and $R_4 = 0.453$ kΩ, **d** $R_1 = 5.683$ kΩ, $R_2 = 5.832$ kΩ, $R_3 = 0.946$ kΩ, and $R_4 = 0.449$ kΩ (Color figure online)

Conclusion

In this paper, the electrical activities in the three-variable Wilson neuron model with the consideration of electromagnetic induction were explored by the numerical simulations and hardware experiments. Herein, the electromagnetic induction effect is equivalent to a flux-controlled memristor applying the membrane potential as the empirical literatures done (Bao et al. 2020b; Ge et al. 2018). The numerical explorations revealed that the proposed Wilson neuron model can generate rich mode transition behavior and asymmetric coexistence of electrical activities in responding to the memristor-related parameters and initial conditions. These numerical explorations reflected that the electromagnetic induction can trigger rich electrical activities in biological neuron. Furthermore, an analog circuit was synthesized and hardware experiments were executed. The phase trajectories and time-domain waveforms were captured from the experimental prototype, and found to be consistent with the numerical simulations of asymmetric coexisting electrical activities. It should be stressed that the analog circuit

implementation for Wilson neuron model has not been reported previously. The designed analog circuit in this paper is more feasible for the integrated circuit (IC) design, which might promote a great convenience to the engineering application of the conductance-dependent Wilson neuron model. Remark that memristive electromagnetic induction flow is introduced into Wilson neuron model to imitate the neuron activities under electrophysiological environment. Some novel results have been numerically found and experimentally verified in analog circuit. However, whether these results are related to the clinical manifestations of neurons under electrophysiological environment deserves to be verified.

Acknowledgements We are very grateful for the valuable comments from the anonymous referees. This work was supported by the grants from the National Natural Science Foundation of China under Grant Nos. 12172066, 61801054, and 51777016, the Natural Science Foundation of Jiangsu Province, China under Grant Nos. BK20160282 and BK20191451, and the Postgraduate Research and Practice Innovation Program of Jiangsu Province, China under Grant No. KYCX20_2547.

References

An XL, Qiao S (2021) The hidden, period-adding, mixed-mode oscillations and control in a HR neuron under electromagnetic induction. Chaos Solitons Fractals 143:110587

Bao BC, Bao H, Wang N, Chen M, Xu Q (2017) Hidden extreme multistability in memristive hyperchaotic system. Chaos Solitons Fractals 94:102–111

Bao BC, Hu AH, Xu Q, Bao H, Wu HG, Chen M (2018a) AC induced coexisting asymmetric bursters in the improved Hindmarsh-Rose model. Nonlinear Dyn 92:1695–1706

Bao H, Liu WB, Hu AH (2018b) Coexisting multiple firing patterns in two adjacent neurons coupled by memristive electromagnetic induction. Nonlinear Dyn 95:43–56

Bao H, Zhu D, Liu WB, Xu Q, Chen M, Bao BC (2020a) Memristor synapse-based Morris-Lecar model: Bifurcation analysis and FPGA-based validations for periodic and chaotic bursting/spiking firings. Int J Bifurc Chaos 30:2050045

Bao H, Hu AH, Liu WB, Bao BC (2020b) Hidden bursting firings and bifurcation mechanisms in memristive neuron model with threshold electromagnetic induction. IEEE Trans Neural Netw Learn Sys 31:502–511

Bao BC, Zhu YX, Ma J, Bao H, Wu HG, Chen M (2021) Memristive neuron model with an adapting synapse and its hardware experiments. Sci China Tech Sci 64:1107–1117

Carpenter CJ (1999) Electromagnetic induction in terms of the Maxwell force instead of magnetic flux. IEE Proc Sci Meas Technol 146:182–193

Chay TR (1985) Chaos in a three-variable model of an excitable cell. Physica D 16:233–242

Chua LO (2015) Everything you wish to know about memristors but are afraid to ask. Radioengineering 24:319–367

Dawson SP, Grebogi C, Yorke JA, Kan I, Koçak H (1992) Antimonotonicity: inevitable reversals of period-doubling cascades. Phys Lett A 162:249–254

FitzHugh R (1961) Impulses and physiological states in theoretical model of nerve membrane. Biophys J 1:445–466

Ge MY, Jia Y, Xu Y, Yang LJ (2018) Mode transition in electrical activities of neuron driven by high and low frequency stimulus in the presence of electromagnetic induction and radiation. Nonlinear Dyn 91:515–523

Gu HG, Pan BB, Li YY (2015) The dependence of synchronization transition processes of coupled neurons with coexisting spiking and bursting on the control parameter, initial value, and attraction domain. Nonlinear Dyn 82:1191–1210

Hindmarsh JL, Rose RM (1982) A model of the nerve impulse using two first-order differential equations. Nature 296:162–164

Hodgkin AL, Huxley AF (1952) A quantitative description of membrane current and its application to conduction and excitation in nerve. J Physiol 117:500–544

Imani MA, Ahmadi A, Malekshahi MR, Haghiri S (2019) Digital multiplierless realization of coupled Wilson neuron model. IEEE Trans Biomed Circuits Syst 12:1431–1439

Jin WY, Wang A, Ma J, Lin Q (2019) Effects of electromagnetic induction and noise on the regulation of sleep wake cycle. Sci China Technol Sci 62:2113–2119

Jiang YN, Huang P, Zhu DB, Han RZ, Liu LF, Liu XY, Kang JF (2018) Design and hardware implementation of neuromorphic systems with RRAM synapses and threshold-controlled neurons for pattern recognition. IEEE Trans Circuits Syst I Reg Papers 65:2726–2738

Kafraj MS, Parastesh F, Jafari S (2020) Firing patterns of an improved Izhikevich neuron model under the effect of electromagnetic induction and noise. Chaos Solitons Fractals 137:109782

Kengne J, Negou AN, Tchiotsop D (2017) Antimonotonicity, chaos and multiple attractors in a novel autonomous memristor-based Jerk circuit. Nonlinear Dyn 88:2589–2608

Li CB, Thio WJ, Sprott JC, Zhang RX, Lu TA (2017) Linear synchronization and circuit implementation of chaotic system with complete amplitude control. Chin Phys B 26:120501

Liu Y, Ma J, Xu Y, Jia Y (2019) Electrical mode transition of hybrid neuronal model induced by external stimulus and electromagnetic induction. Int J Bifurc Chaos 29:1950156

Lv M, Wang CN, Ren GD, Ma J, Song XL (2016) Model of electrical activity in a neuron under magnetic flow effect. Nonlinear Dyn 85:1479–1490

Ma J, Tang J (2017) A review for dynamics in neuron and neuronal network. Nonlinear Dyn 89:1569–1578

Manimehan I, Philominathan P (2012) Composite dynamical behaviors in a simple series–parallel LC circuit. Chaos Solitons Fractals 45:1501–1509

Mondal A, Upadhyay RK, Ma J, Yadav BK, Sharma SK, Mondal A (2019) Bifurcation analysis and diverse firing activities of a modified excitable neuron model. Cogn Neurodyn 13:393–407

Morris C, Lecar H (1981) Voltage oscillations in the barnacle giant muscle fiber. Biophys J 35:193–213

Nouri M, Hayati M, Serrano-Gotarredona T, Abbott D (2019) A digital neuromorphic realization of the 2D Wilson neuron model. IEEE Trans Circuits Syst II Express Briefs 66:136–140

Parastesh F, Rajagopal K, Karthikeyan A, Alsaedi A, Hayat T, Pham VT (2018) Complex dynamics of a neuron model with discontinuous magnetic induction and exposed to external radiation. Cogn Neurodyn 12:607–614

Pinto RD, Varona P, Volkovskii AR, Szücs A, Abarbanel HD, Rabinovich MI (2000) Synchronous behavior of two coupled electronic neurons. Phys Rev E 62:2644–2656

Qi Y, Watts AL, Kim JW, Robinson PA (2013) Firing patterns in a conductance-based neuron model: bifurcation, phase diagram, and chaos. Biol Cybern 107:15–24

Rostami Z, Jafari S (2018) Defects formation and spiral waves in a network of neurons in presence of electromagnetic induction. Cogn Neurodyn 12:235–254

Steyn-Ross DA, Steyn-Ross ML, Wilson MT, Sleigh JW (2006) White-noise susceptibility and critical slowing in neurons near spiking threshold. Phys Rev E 74:051920

Steyn-Ross ML, Steyn-Ross DA (2016) From individual spiking neurons to population behavior: systematic elimination of short-wavelength spatial modes. Phys Rev E 93:022402

Wang Y, Ma J, Xu Y, Wu FQ, Zhou P (2017) The electrical activities of neurons subject to electromagnetic induction and Gaussian white noise. Int J Bifurc Chaos 27:1750030

Wilson HR (1999) Simplified dynamics of human and mammalian neocortical neurons. J Theor Biol 200:375–388

Wu FQ, Wang CN, Xu Y, Jun M (2016) Model of electrical activity in cardiac tissue under electromagnetic induction. Sci Rep 6: Article no. 28

Wolf A, Swift JB, Swinney HL, Vastano JA (1985) Determining Lyapunov exponents from a time series. Physica D 16(3):285–317

Xu Q, Lin Y, Bao BC, Chen M (2016) Multiple attractors in a non-ideal active voltage-controlled memristor based Chua's circuit. Chaos Solitons Fractals 83:186–200

Xu Y, Ma J, Zhan X, Yang LJ, Jia Y (2019) Temperature effect on memristive ion channels. Cogn Neurodyn 13:601–611

Xu Q, Tan X, Zhu D, Bao H, Hu YH, Bao BC (2020) Bifurcations to bursting and spiking in the Chay neuron and their validation in a digital circuit. Chaos Solitons Fractals 141:110353

Yang YM, Ma J, Xu Y, Jia Y (2020) Energy dependence on discharge mode of Izhikevich neuron driven by external stimulus under electromagnetic induction. Cogn Neurodyn 15:265–277

Ye WJ, Mai WD, Hu GW (2018) Effects of the electromagnetic radiation on cognitive performance: a model study. Nonlinear Dyn 93:2473–2485

Zhao X, Kim JW, Robinson PA, Rennie CJ (2013) Low dimensional model of bursting neurons. J Comput Neurosci 36:81–95

Zhou L, Wang CH, Zhang X, Yao W (2018) Various attractor, coexisting attractors and antimonotonicity in a simple fourth order memristive Twin-T oscollator. Int J Bifurc Chaos 28:1850050